Published in final edited form as:
J Appl Physiol. 2008 May ; 104(5): 1495–1503. doi:10.1152/japplphysiol.01005.2007.

Role of collateral paths in long-range diffusion in lungs

Seth-Emil T. Bartel[1], **Susan E. Haywood**[2], **Jason C. Woods**[1], **Yulin V. Chang**[1], **Christopher Menard**[1], **Dmitriy A. Yablonskiy**[1,2], **David S. Gierada**[2], and **Mark S. Conradi**[1,2]

[1] Department of Physics, Washington University, St. Louis, Missouri

[2] Department of Radiology, Washington University, St. Louis, Missouri

Abstract

The long-range apparent diffusion coefficient (LRADC) of ^{3}He gas in lungs, measured over times of several seconds and distances of 1–3 cm, probes the connections between the airways. Previous work has shown the LRADC to be small in health and substantially elevated in emphysema, reflecting tissue destruction, which is known to create collateral pathways. To better understand what controls LRADC, we report computer simulations and measurements of ^{3}He gas diffusion in healthy lungs. The lung is generated with a random algorithm using well-defined rules, yielding a three-dimensional set of nodes or junctions, each connected by airways to one parent node and two daughters; airway dimensions are taken from published values. Spin magnetization in the simulated lung is modulated sinusoidally, and the diffusion equation is solved to 1,000 s. The modulated magnetization decays with a time constant corresponding to an LRADC of ~0.001 cm^2/s, which is smaller by a factor of ~20 than the values in healthy lungs measured here and previously in vivo and in explanted lungs. It appears that collateral gas pathways, not present in the simulations, are functional in healthy lungs; they provide additional and more direct routes for long-range motion than the canonical airway tree. This is surprising, inasmuch as collateral ventilation is believed to be physiologically insignificant in healthy lungs. We discuss the effect on LRADC of small collateral connections through airway walls and rule out other possible mechanisms. The role of collateral paths is supported by measurements of smaller LRADC in pigs, where collateral ventilation is known to be smaller.

Keywords

gas magnetic resonance imaging; hyperpolarized; collateral ventilation

The development of hyperpolarized noble gases, ^{3}He and ^{129}Xe, has allowed the magnetic resonance visualization and characterization of these gases in the air spaces of lungs (17,25). The first applications were so-called ventilation imaging, revealing the distribution of polarized gas upon inhalation of a bolus of gas followed by breath hold or during several breaths. Subsequently, diffusion MRI of hyperpolarized ^{3}He was shown to be a powerful method for characterizing the microstructural changes to the lung in emphysema (6,28,29). The airway and alveolar walls restrict the random Brownian motion of the gas; airway expansion and tissue destruction result in less restriction. Most measurements have used diffusion times of 1–10 ms, corresponding to free gas displacements on the order of 0.5 mm; we call these short-range apparent diffusion coefficients (SRADC). Measurements with typically two values for weight of the diffusion-sensitizing gradient pulses (*b*) are fitted to exponential decays and report small SRADC in health (typically 0.2 cm^2/s; compare with a

Address for reprint requests and other correspondence: M. S. Conradi, Washington Univ., Dept. of Physics-1105, One Brookings Dr., St. Louis, MO 63130 (MSC@wuphys.wustl.edu).

free diffusivity of the same ^{3}He diluted in N_2 or air of 0.88 cm^2/s) and substantially higher SRADC in emphysema (0.6 cm^2/s is typical of severely diseased regions) (28).

The understanding of short-range restricted diffusion was strengthened by a theory using a model of cylindrical airways in which the SRADC is a tensor, with principal values D_L and D_T describing diffusion longitudinal and transverse to each acinar airway, respectively (40). In each imaging voxel, the airways are oriented essentially equally in all directions; the result of this microscopic diffusion anisotropy with macroscopic isotropy is a nonexponential signal decay as a function of *b*. The nonexponential decay has also been treated phenomenologically using the formalism of kurtosis (12).

More recently, long-range diffusion measurements have been reported using spatially modulated (or tagged or striped) longitudinal spin magnetization (1) with a striping wavelength (λ) of 2–3 cm; diffusion over times of seconds attenuates the modulation by smearing across the peaks and troughs of the modulation (18,27). It is as though the ^{3}He atoms are painted white or black (magnetized or not) in a striped pattern, and one measures the rate at which they subsequently mix to appear gray. These measurements can thus be regarded as probes of displacements of approximate length λ/2, with λ chosen so that the stripe pattern decays appreciably before the spin magnetization has substantially decayed through T_1 processes. In healthy in vivo and explanted lungs, long-range apparent diffusion coefficient (LRADC) values near 0.02 cm^2/s for λ = 2 cm, a factor of ~10 smaller than SRADC, have been reported (27,38). The stimulated echo method of Wang et al. (33) also modulates the longitudinal magnetization, but in the direction of the slice thickness, allowing λ to be varied over a wide range. For λ = 2 cm, those data from healthy volunteers are in accord with the above-mentioned LRADC value. The quantities SRADC and LRADC have also been named D_{msec} and D_{sec}, respectively, expressing the relevant time scales.

In emphysema, large increases in LRADC have been reported; expressed as a ratio, the increases in LRADC are generally larger than those in SRADC (18,33,34). This suggests that LRADC may be a more sensitive indicator of emphysematous changes in lung microstructure than SRADC. Holes in airway walls, or the eventual annihilation of the walls in severe disease, provide additional, collateral paths for movement of the gas (24,36). For the present purposes, collateral paths are defined as any routes available for gas motion that are not described by the canonical model of branching airways (35,37). We believe the increases in LRADC reflect enlargement or creation of collateral paths due to tissue destruction that is prominent in emphysema.

Our goal is to better understand what the LRADC implies about the structure of the lung. That is, what aspects of lung microstructure control the LRADC? As a step toward that goal, we report computer simulations and new measurements of ^{3}He LRADC in healthy lungs. Our aim is to provide a definite model through which LRADC measurements can be understood, much as the cylindrical airway model (40) is a framework for understanding SRADC. The present computer simulations represent only the canonical airway tree (35,37); the results imply that the omitted collateral paths play an important role in LRADC.

METHODS

Computer simulations

Overall, we calculate the diffusion of ^{3}He spin magnetization up and down the airways. The airways are narrow compared with λ, so the airways are treated as line segments. The important issue is the progress of the diffusing spins along the direction of the striping gradient; this progress depends on how the airways are distributed in space.

The simulation routines were written in the language C++ and performed on a personal computer. The simulations started with generation of a three-dimensional (3D) lung structure as a network of nodes (junctions) in space, with each node (level Z) connected by airways to a parent node (level $Z - 1$) and two daughter nodes (level $Z + 1$) (37). The airway radii and lengths were selected from published values for the symmetrical branching model of human lung (Table 1 of Ref. 35). Lung generation typically started with $Z = 5$ airway ($Z = 0$ is the trachea), because we reasoned that, for $\lambda = 2$ or 3 cm, it is not necessary to create a complete, full-size lung; for example, no diffusion paths relevant to 2-cm displacements will involve the trachea. By starting at $Z = 5$, instead of $Z = 0$, the number of nodes and amount of computing time needed to capture displacements on the order of 2 cm are reduced by a factor of 2^5. The simulated lungs used the bifurcating, symmetrical branching geometry (9,35) shown in Fig. 1. An airway of level Z extends from a level $Z - 1$ node to a level Z node. Symmetrical branching through half-angle (θ) occurs, giving rise to two level $Z + 1$ airways terminating at level $Z + 1$ nodes; typically, $\theta = 40°$ but, occasionally, varied from 35° to 45°. The parent and two daughter airways are co-planar, with the rotation angle (φ) of the plane about the parent airway selected at random from 0° to 360°. The lung generation procedure starts at a single, lowest-level airway and continues to the $Z = 14$ nodes, which are the acini (the gas-exchanging units).

An acinus (9,14,30,37) typically extends from $Z = 14$ (just beyond the terminal bronchioles) to $Z = 23$, with a volume of 185 mm^3, corresponding to a linear size of ~6 mm (a compact structure). Inasmuch as this is small compared with λ, we chose to represent acini as point objects, suppressing their internal structure. Nevertheless, in the model, each acinus was given a gas volume of 185 mm^3, with recognition that 93% of the gas in human lungs resides in acini. This lung generation scheme is neither self-avoiding nor space filling.

Diffusion along the simulated branching airway structure was treated with discrete equations, in which all the gas in a level Z airway and its level Z node (Fig. 1) is assigned the position of the level Z node. This greatly reduces the required computational steps and is a good approximation, because the airway radii and lengths are small compared with the relevant length scale of λ (with the exception of the few smallest Z airways). In effect, the branching airway network is equivalent to the electrical resistor-capacitor (RC) network of Fig. 2. The resistors are the airways along which gas diffuses, and the capacitors represent the volumes of gas concentrated at each node. Although Fig. 2 has the correct branching connectivity, the location of the airways and nodes in three-dimensional space is more complicated, with elements of randomness as in Fig. 1. Crucially, the magnetic field gradient in the stripe-generating portion of the pulse sequence works on the location of spins in 3D space.

Table 1 presents analogous quantities and equations relating the worlds of spin magnetization and the electrical RC network of Fig. 2. The conserved quantities during time evolution are the total spin magnetic moment (μ; here we omit T_1 processes, since these are removed in data analysis of real measurements) and the electrical charge (q). Diffusion is driven by differences in magnetization (M, i.e., magnetic moment per volume) between neighboring nodes (i.e., ΔM), analogous to differences in electrical potential [i.e., voltage (V)]. The flow of diffusing magnetic moments is thus governed by an equation analogous to Ohm's law, $I = \Delta V/R$, as listed in Table 1. Because the airways at levels lower than 14 (i.e., not acinar airways) are essentially smooth-walled cylinders, their areas (A) were taken as πR^2 and the free diffusivity (D) of ^{3}He diluted in N_2 or air (40) was used: $D = 0.88$ cm^2/s.

The simulated lungs were initially filled with uniform spin magnetization (M) by setting M = 1 at every node and acinus. This was then spatially modulated, yielding $M = \cos(\vec{k}\cdot\vec{r} + \theta)$, where $\vec{r}$ is the 3D position of the node, M is its magnetization, and $\vec{k} = \hat{n}2\pi/\lambda$, where $\hat{n}$ is the

randomly selected direction of striping for the lung. The phase shift (θ) is selected randomly for each lung, from 0 to 2π. The diffusion equation for the discrete network was then solved as follows

$$M^{new}=M^{old}+(dM/dt)\Delta t \quad (1)$$

where Δt is the time step. The value of dM/dt at each node is calculated according to Table 1

$$\frac{dM}{dt}=\frac{1}{V}I_{tot}=\frac{1}{V}(I_P+I_{D1})+I_{D2}) \quad (2)$$

where V is the volume of the node and its airway and the diffusion currents (I) refer to flow into the node from the parent (P) and two daughters (D1 and D2; Figs. 1 and 2). For acini, which are terminal units, there are no daughters, so these currents are zero. M at each node was archived for later analysis at each time step. In that analysis, μ at each value of the coordinate n ($n = \vec{k}\cdot\vec{r}/|k| = \hat{n}\cdot\vec{r}$, the projection of $\vec{r}$ onto the gradient direction) was collected as a histogram. Typical histograms are presented in Fig. 3 for 0, 100, and 500 s after initial striping.

Δt was chosen to be smaller than the shortest time constant of the system (i.e., describing motion between neighboring nodes) to avoid instability (overshoot and oscillation) of the solution. On the other hand, selection of excessively small Δt increases the required computer time for a given amount of simulation time. In the airway tree, Δt = 25 ms was used; for simulations of the acinus where internal time constants are shorter, Δt of 1 ms was used. In all cases, we ensured that the solutions were convergent and that identical results were obtained with smaller Δt.

The amplitude (S) of the Fourier coefficient of the striped magnetization was computed at each time t as a simple Fourier sum corresponding to the striping waveform

$$S=2\sum_{\text{node } j} M_j V_j \cos k n_j / \sum_{\text{node } j} V_j \quad (3)$$

where V_j is the volume associated with the jth node, located at $n_j = \hat{n}_j\cdot\vec{r}_j$, and M_j is its spin magnetization. The factor of 2 ensures that S = 1 at t = 0. It was found that S decays with increasing time because of diffusion of the ^{3}He between regions of low and high M. An initial rapid decay of the first 10% (S from 1 to 0.9) is due to the much faster motion through large airways. By restriction of the sums in Eq. 3 to only the acinar nodes, the initial rapid decay was suppressed; the more slowly decaying signal was unaffected. The decay proceeds toward a state in which M is uniform (and small) across the lung. The somewhat uneven distribution of nodes along the coordinate axis n (Fig. 3) results in the total μ (which remains constant) being slightly different from zero. This constant was subtracted from all data sets of S.

The lungs generated by the algorithm had random features [the angles (φ) in Fig. 1 at every node], so an averaging over 32 similarly generated lungs was always used.

An "evolution" algorithm was used to improve the uniformity of space filling of the simulated lungs. The algorithm attached point scores to regions of excessive density (i.e., alveoli within 5.7 mm of each other, with 5.7 mm being the cube root of the assumed alveolar volume of 185 mm^3) and to regions devoid of alveoli. A set of 32 candidate lungs was ranked in this way. Branches were swapped randomly to improve the space filling of the lungs. In detail, for each round of swaps, a branching level was selected randomly. Branches of the selected level from other lungs were transferred to the given lung after translation and rotation (so that the lowest-numbered elements of the transferred branch match those of the replaced branch). Score-reducing changes were retained, and score-increasing changes were discarded. Approximately 80 rounds of such swapping produced lungs with improved space filling, as indicated by their lower point scores. The long-range diffusion was measured on the most improved lungs by following the decay of modulated magnetization. Change in the decay time constant (an increase of <5%, which is small compared with lung-lung variations) was negligible compared with the original lungs. The "evolved" lungs were not pursued further.

Measurements

LRADC was measured at 1.5 T in Siemens Vision and Sonata MRI scanners. Home-built Helmholtz-like radiofrequency (rf) coils were placed underneath the back and on top of the chest of supine volunteers. For explanted lungs, a solenoid coil oriented perpendicular to the static magnetic field was used. Striping was applied with two rectangular 45° rf pulses separated by a gradient pulse in the anterior-posterior direction (18). λ is determined by the condition $\gamma G\delta\lambda = 2\pi$, where γ is the magnetogyric ratio of ^{3}He, G is the gradient amplitude, and δ is the equivalent rectangular pulse width. The evolution of the striped magnetization was measured with multislice, two-dimensional FLASH images obtained every 2 s; typically, four transverse 2-cm-thick slices were captured. The images used a field of view of 450 × 225 mm, a matrix of 64 × 32, in-plane voxels of 7 × 7 mm, and an rf pulse flip angle of 5° to allow repetitive imaging from the same slices. The analysis of the images to follow the decaying amplitude of the stripes has been described elsewhere (18) and is automatically corrected to eliminate effects of T_1 relaxation and consumption of the longitudinal magnetization by previous rf imaging pulses. Thus the striping decay reflects only long-range diffusion, transporting spins between regions of high and low magnetization. The analysis software reports a decay rate constant (R) for the striping centered at each image voxel by fitting a single-exponential decay [$\exp(-Rt)$] to the striping relative amplitude (called the fractional modulation). Finally, R is converted to an LRADC value by

$$R=(\mathrm{LRADC})k^2 \quad (4)$$

a relation that is based on Gaussian diffusion (23); here $k = 2\pi/\lambda$.

Three male and one female volunteers who had never smoked (26 ± 3 yr of age) were selected. The imaging procedures and the informed consent process were approved by the Washington University Human Studies Committee. The use of ^{3}He is performed under a US Food and Drug Administration investigational new drug exemption. Five normal donor lungs (3 male and 2 female, 27 ± 7 yr old) that could not be matched to a recipient or could not be used for other reasons were obtained through the Washington University Lung Transplant Program. The lungs were fitted with a tubing connection and stored over cold saline. The explanted lungs were thoroughly purged with N_2 before imaging (38) to reduce the decay rate (T_1^{-1}) of the hyperpolarized ^{3}He from O_2, which is paramagnetic and highly relaxing (17,25).

The ^{3}He gas was polarized (17) using home-built polarizers in the Washington University Department of Physics, providing up to three 0.45-liter STP boli each at typical polarizations of 35–40%. The polarized ^{3}He was mixed with ~1.5 liters of N_2 in a plastic bag to provide a full inhalation to near total lung capacity; for the explanted lungs, the total volume was ~1 liter. On two occasions, gas was polarized with a General Electric polarizer in the same building as the magnetic resonance scanner. Following verbal instructions, the volunteer inhaled the gas from the bag through a flexible tube and held his/her breath; imaging commenced then and continued for 6–10 s. With explanted lungs, the gas mixture was delivered by a calibrated gas syringe.

Long-range diffusion was also measured in pig lungs for comparison with the human results. These lungs were handled and imaged with the same techniques used for explanted human lungs, but with smaller volumes of gas (~0.5 liter total bolus). Freshly harvested left lungs were obtained from three pigs killed for cardiology experiments, with all procedures approved by the Washington University Animal Studies Committee. A fixed left-right pair of lungs from one pig was purchased from a biological supply house (Nasco).

RESULTS

Acinus

Before turning to the simulation results of LRADC in the simulated lungs, we address the modeling of the acinus as a single RC equivalent unit. As shown below, the time constants of the model acini are much shorter than the overall decay time constant of the stripes (23 vs. 110 s), demonstrating that the bottleneck to long-range diffusion resides outside the acini. This permits a considerable simplification in the simulations, with the single RC unit replacing ~10 branching levels and 1,023 nodes of the actual acinus. This simplification also rests on the linear size of the acini (~6 mm) being smaller than the relevant length scale (λ, which is always ≥2 cm).

We model the acinus (9,30) using the RC branching network of Fig. 2, starting at $Z = 14$ and with 10 levels of nodes and a time step of 0.001 s. The total volume is 185 mm^3, and the airway radii and lengths are taken from the literature (Table 2 in Ref. 9). The radius that was chosen is the major radius, which includes the sleeve of alveoli. The diffusive conductance of the airway, $1/R = DA/L$ from Table 1, used the free diffusivity $D_0 = 0.88$ cm^2/s for ^{3}He diluted in air or N_2 for $Z = 14$–16, where alveolarization is not complete. The higher-numbered airways are more completely covered by alveoli; there the diffusivity was taken as 0.44 cm^2/s (although the acinar time constant is very insensitive to this value). This value is from ^{3}He MRI measurements of D_L in healthy volunteers (40). Only the progress of spins over long distances matters here, so D_T is of no importance.

To determine the acinar diffusive behavior, the model acinus was filled with uniform magnetization M = 1 at *time 0*, equivalent to a uniform unit voltage on each capacitor. Free diffusive exhaust, corresponding to the acinus inlet being opened to free air, is equivalent to discharging the RC network by grounding the left-hand side of the input resistor (i.e., voltage there clamped to zero). The decay of the total spin magnetic moment is presented in Fig. 4, along with a best-fit single-exponential decay [$A\cdot\exp(-R't)$]. The decay time constant $1/R'$ is ~23 s. This result can be modeled by a single RC element, with C corresponding to the total volume of 185 mm^3 and R selected to yield the correct time constant (τ), with $RC = \tau$.

It is easy to show by electrical network analysis that the single RC element is the correct approximation to the acinus of Fig. 2 in the limit of low frequencies (corresponding to the slow decay of the modulated magnetization in the overall lung). In particular, the single

capacitance should account for the total charge (and, hence, be equal to the total actual capacitance); the single resistor accounts for the power dissipation in the low-frequency limit. This analysis results in the value of the resistance of the single RC equivalent being ~1.5 times the input resistance of the actual network of Fig. 2, a result in agreement with the decay time constant in Fig. 4. Very roughly, the input resistance of the network in Fig. 2 substantially controls the discharge, because all the discharge current is "funneled" through this one element; the other resistors each carry only fractions of the total current.

The acinar decay time constant varies reciprocally with the gas diffusivity, so the slower diffusion of O_2 or CO_2 through air would result in a longer time constant. If the acinus were smaller (e.g., starting at $Z = 15$), its volume and time constant would be smaller. The overall lung simulations used acini at $Z = 14$ represented by the single RC network with volume = 185 mm^3 and $\tau = 20$ s.

A recent publication (32) simulates diffusion over times of seconds in single human acini. The authors find a component with a relatively long time constant of equilibration of concentration; by comparison with the time constant in a reference (trumpet) structure, the effective diffusivity of 0.01 cm^2/s is determined. This value is noted to be in reasonable agreement with measured LRADC in normal human lungs. However, the simulations involve undetermined distances, but these are surely no larger than the linear size of acini (~6 mm). Thus, although the simulations (32) may be relevant to the decay of shorter-wavelength stripes, they cannot describe the decay of modulated magnetization with wavelengths of 2 and 3 cm. This conclusion is supported by calculations in the Appendix.

Decay of modulated magnetization

The decay of the modulated magnetization in a representative simulated lung is presented in Fig. 5, where $\lambda = 2$ cm was used. The simulation data S have been fitted to a single-exponential decay [$S \sim \exp(-Rt)$] in Fig. 5, with time constant 110 s. It is clear that the data do not decay with a single decay constant; instead, S decays more rapidly initially and more slowly over the long term. In MRI measurements at Washington University reported here and elsewhere (18,38), the signal-to-noise ratio did not warrant an analysis in terms of multiple decay rates, so the single-exponential decay is used to describe the present simulation results. The stimulated echo results show a decreasing LRADC with increasing time, in agreement with our simulations (33). Using Eq. 4 to relate the decay rate constant R to the LRADC, we find LRADC = 0.0009 cm^2/s (±10%). Equation 4 is strictly applicable only for Gaussian diffusion. However, inasmuch as our intention is to compare the simulation results with experimental measurements, use of Eq. 4 to describe both data sets is justified. Thus comparison of the simulated and measured LRADC is equivalent to comparing the decay rate constants R (which are the directly determined quantities).

Similar decays have been obtained with many sets of 32 lungs with $\theta = 35–45°$, with very nearly equal average values of LRADC, varying only by ±10%. Our simulations were limited to $\lambda \geq 2$ cm because of our pointlike representation of the acini. Very large λ would present edge-effect artifacts arising from the simulated lungs not being many wavelengths long in the striping direction (Fig. 3). Thus we used only $\lambda = 2$, 3, and 4 cm. The decay time constant for $\lambda = 3$ cm averaged near 194 s, implying an LRADC of 0.0012 cm^2/s. For $\lambda = 4$ cm, the observed time constant of 310 s corresponds to an LRADC of 0.0013 cm^2/s. All time constants and LRADC values showed a standard deviation of ~10% across the sets of 32 lungs. The observed overall time constants are much longer than the acinar time constant of 20 s, indicating that the overall result is insensitive to the detailed treatment of the acini. This was confirmed by varying the acinar time constant from 10 to 20 s and observing only insignificant changes in the overall decay time constant of the stripes.

For the simulated lungs with λ = 2 cm magnetization modulation, we investigated which nodes participated in the diffusion paths. Lungs were modified by closing all the airways [setting their diffusive conductances (1/*R*) to 0] at (and only at) a specific airway level *Z*; airways at all other levels were unchanged. Decays of the modulated magnetization amplitude S are presented in Fig. 6 for a normal simulated lung as well as lungs with closed airways for (separately) *Z* = 8, 10, and 12. The decay of S is essentially blocked by closure of all *Z* = 12 airways, while closing the *Z* = 8 or 10 airways has relatively little effect on the decay (compared with the normal lung). We recall that most of the volume in the lung is in the acini and that the quantity S is obtained only from the acinar magnetization. Thus the results of Fig. 6 describe the diffusion paths relevant to the decay of modulated signal S, from one acinus to another. Evidently, nearly all the relevant paths pass through *Z* = 12 airways, and few pass through *Z* = 8 or 10 airways. The simulation results of Fig. 6 provide strong support that the lungs simulated by starting at *Z* = 5 are sufficiently large to capture diffusion over the distances relevant to the wavelengths employed. For much larger λ, one would expect a lower-numbered critical airway level.

Magnetization-tagged images of an explanted normal donor lung and an in vivo healthy volunteer are presented in Fig. 7. In both cases, λ = 2.0 cm and the fields of view are 320 and 448 mm, respectively. At *t* = 0, just after striping, the modulation is very strong; later at *t* = 5.8 s (the last in a series of images), the modulation has decayed noticeably, particularly in certain regions.

At each pixel, *R* of the fractional modulation, as well as LRADC, is determined from Eq. 4 (Fig. 7). Considerable variation of LRADC is apparent across both lungs. We note the much larger LRADC in the apices of the volunteer's lungs, which is also evident in the near absence of remaining modulation at *t* = 5.8 s in those regions.

Long-range diffusivity data from the explanted and in vivo measurements are summarized in Table 2. The whole lung average of LRADC, as well as its averages over the apical and basal regions [upper third and lower third of lung(s), respectively] is given. Although the number of values reported is not large, certain trends appear. *1*) In every case, the diffusivity is larger in the apical region than the whole lung average and the basal region average. *2*) There is substantial variation in diffusivity between individuals. *3*) In the two cases measured, the long-range diffusivity is larger at a larger lung volume (comparing within a given subject at two lung volumes). The data also suggest that the average diffusivity may be higher in the volunteers than in the explanted normal lungs. However, given the sensitivity of the results to the level of lung inflation, we regard this finding with caution, inasmuch as the in vivo and ex vivo measurements were likely at different levels of inflation. One volunteer was found to be asthmatic; therefore, data from this subject do not appear in Table 2. The average LRADC values for this subject were unusually low (0.008 cm^2/s across the lungs, 0.010 in the apices, and 0.004 in the basal region).

DISCUSSION

The simulation results for decay of modulated spin magnetization display a much slower decay rate constant, near 0.01 s^{-1}, and smaller resulting LRADC, near 0.001 cm^2/s, than the measurements of LRADC in normal human lungs reported here in Table 2 and elsewhere (18,27,33,38). We emphasize that the measured LRADC values are ~20 times larger than the simulated values. The simulation results were insensitive to variations in θ over the physiological range of 35–45° (35). The lungs were generated with a random algorithm, but large variations among the decay in the 32 lungs in each set were not found. In addition, the time constants of the acinar units were found to be small compared with the overall time for decay of the modulation (20 vs. 110 s), indicating that the details of how the acini are

modeled do not have much effect on the overall striping decay. The simulations behave in the manner expected with respect to airway closures: closing all airways at level $Z = 8$ or 10 had little effect on the decay of the stripes, whereas closure of the $Z = 12$ airways blocked most of the decay

So we must consider whether the measured LRADC values are artificially high. We note that diffusion yields a root mean square displacement (23) proportional to $\sqrt{t}$, whereas flow (convection) displacements over short times are linearly proportional to t. Thus, at short times (as in measurements of short-range diffusivity), the diffusive displacements generally dominate; indeed, there have been no reports of flow artifacts in the many measurements of SRADC with ^{3}He gas (7,26,28,29). At long times, such as used here, the flow displacements may become more important relative to the diffusive motions. One obvious possibility of flow or motion artifacts would be lack of complete breath hold. In addition to the overall motion of each lung region (which would move the stripes in the image without decreasing their amplitude), flow of gas through the airways would result in attenuation of the stripes. A second possible source of stripe decay would be gas flow induced by the beating heart (cardiogenic mixing). Of course, lack of breath hold and cardiogenic mixing are absent in the explanted lungs, so these effects cannot explain the large difference between the simulated and measured long-range diffusivities. A recent study of lung motion using tagged ^{3}He magnetization found that the tagging remained surprisingly prominent after exhalation (4).

What role does solubility of the ^{3}He gas play in transporting the ^{3}He nuclear spins through the airway walls, instead of along the airways? To address this mechanism, we computed the LRADC of a periodic structure with parallel, infinite planar walls of thickness δ spaced by length l. The Ostwald solubility (defined as the dimensionless ratio of concentration of ^{3}He in the wall divided by the gas-phase concentration at equilibrium) is p and ^{3}He dissolved into the wall has diffusivity D_W. Then a simple calculation with a steady flux of ^{3}He through the structure and a constant concentration gradient (averaged over distances greater than l) yields

$$\frac{1}{\mathrm{LRADC}} = \left(1 - \frac{\delta}{l}\right)\frac{1}{D_o} + \left(\frac{\delta}{l}\right)\frac{1}{p\mathrm{D_w}} \tag{5}$$

This is essentially an analogy to an electrical series circuit. We use $D_o = 0.88$ cm^2/s, $p = 0.96 \times 10^{-2}$ for He in water [(19) in the airway walls], and $D_W = 10^{-4}$ cm^2/s [a factor of 4 higher (13) than the self-diffusion of water], with typical lung tissue parameters (37) of $\delta = 10$ μm and $l = 0.5$ mm. For these values, the second term dominates the first term by a factor of 10^4, leading to

$$\mathrm{LRADC} = D_w p(l/\delta) \tag{6}$$

or LRADC = 0.5×10^{-4} cm^2/s, which is clearly negligible compared with the measured and simulated values of LRADC.

A related possible mechanism, available only in vivo, is solution of ^{3}He into the capillary blood in the alveolar walls, transport with the flowing blood, and (at some distant location) reentry into the gas phase. This effect cannot reconcile the values of LRADC measured in explanted lungs (Table 2) with the simulation results, of course.

Collateral ventilation paths (24) have long been recognized and constitute all paths that are not described by the canonical branching airway tree. Interalveolar pores of Kohn have been reported in alveolar walls; whether emphysematous tissue destruction begins by enlargement of these pores (24) and whether these pores are normally open or fluid filled have been discussed (2). Bronchoalveolar channels of Lambert (16) and interbronchiolar channels of Martin (22) also exist. Collateral paths offer a parallel set of routes for long-range gas diffusivity; because the collateral paths pass through airway walls, they can be regarded as short circuits. Indeed, these are more direct paths, so they avoid the tortuosity of paths that follow the airways. It is believed that collateral paths serve a functional purpose in disease, allowing ventilation of regions with a direct airway supply that has become plugged (5,31).

The measured values of LRADC, both in vivo and ex vivo, are ~20 times greater than the simulated diffusivities. We believe this is because real normal human lungs have collateral pathways that are functional, whereas the simulations treat only the canonical airway tree.

A large fraction of the present knowledge of collateral ventilation paths has come from the wedged catheter technique (11,20,24,31), whereby a catheter supplies airflow to a lung airway while sealing the airway to prevent the gas from escaping past the catheter. If the only paths were the bifurcating network of singly connected airways, no gas could flow in this arrangement at steady state. However, gas supplied by the catheter finds collateral paths into other lung regions not served directly by the now-blocked airway.

A major conclusion from the wedged catheter studies is that, in health, collateral path resistance is much greater than resistance along the airways proper (5,10,21,31). For example, Macklem (20) wrote, “for it is by no means certain that collateral ventilation plays any important role in the function of normal lungs.” However, in emphysema, wholesale tissue destruction occurs with a massive increase in collateral paths (5,31). We note two important points concerning the relative unimportance of collateral ventilation in health. First, most of the work has used $Z = 3–6$ for the location of the wedged catheter; use of higher-numbered airways is difficult because of their small size. So the collateral flow resistance measurements have been at much larger, more proximal airways than are crucial to the long-distance diffusion paths probed here ($Z = 10–12$; Fig. 6).

Second, collateral flow and diffusion obey different scaling relations. As shown in Table 1, the diffusive conductance of a cylindrical connection of length L and cross-sectional area A is DA/L. For the same (round) tube, the flow conductance (quantity per time per unit pressure drop) is proportional to A^2 (fourth power of radius) for laminar flow (15). Thus a large number of very small-radius holes through an airway wall present a small flow conductance and a comparatively larger diffusive conductance. This is one way that a given set of collateral paths could have a major impact on long-range diffusivity (compared with the airway paths) and yet exhibit a flow resistance much greater than the airways.

Finally, we address the number and size of pores required in the airway walls to explain the excess long-range diffusion found here. We consider once more an array of parallel walls (sheets) spaced by distance l; we calculate the diffusion in the direction perpendicular to the walls due to a uniform network of holes (3). The holes are each of radius r with number per unit area n; the holes are assumed to be well separated. Application of the diffusion equations in Table 1 to the individual holes, making use of the fact that the effective cylindrical length of each hole is approximately r, yields the total current through the wall. Taking the averaged flux across each wall and the average concentration (or magnetization) gradient over lengths much larger than the wall spacing l, one finds

$$\mathrm{LRADC}=2nD_{\mathrm{o}}rl \quad (7)$$

We emphasize that this LRADC is much larger than D_o times the fraction of each wall occupied by pores. This result has been confirmed by diffusion simulations (8).

For the present purposes, we note that an array of holes with r = 5 μm forming a square lattice 0.55 mm on a side, with wall spacing l = 0.6 mm, results in LRADC/D_o of ~0.02, which is measured here in lungs in vivo and ex vivo. These parameters mean that the holes occupy only 2.6×10^{-4} of the wall area, a very small fraction. We emphasize that we do not state that the data imply that pores of this size and density are actually present in lung. Rather, with such a seemingly small density of relatively small pores spread across all the airway walls, the anomalously high long-range diffusion measured experimentally in normal lungs is explained.

Pigs are known to have little or no collateral ventilation (20,39), and the pores of Kohn are less numerous in the interal-veolar walls of pigs than in human and canine lungs (20). Thus we measured LRADC in three freshly excised pig lungs and a fixed pig lung. Using a wavelength of 2.1 cm, we found mean LRADC to be 0.0051, 0.0039, and 0.0040 cm^2/s, with 0.0048 cm^2/s in the fixed lung (Table 2). The consistent finding of smaller long-range diffusivity in pig lungs supports our contention that long-range diffusion in healthy human lungs occurs primarily through collateral paths. The SRADC (with diffusion time of 2 ms) was measured in vivo in two pigs, and the mean values of 0.12 and 0.13 cm^2/s (±10%) are only ~60% of the typical value in normal humans.

The calculations and simulations presented here use lung models that could be improved. *1*) Collateral paths could be incorporated directly into the lung model, instead of separate treatment of these paths, as in the discussion leading to Eq. 7. The dependence of the simulated LRADC on the size and number density of collateral paths predicted by Eq. 7 could be confirmed. The dependence on the location of the pores or paths could be determined, information not contained in the present result. *2*) A more accurate model of the airway geometry in space could be used. We believe that a 3D latex casting of an actual lung could be used to determine the coordinates of the airway nodes. *3*) Continuation of the airway simulation into the acini would eliminate the simplification used here (in which acini are treated as points).

Acknowledgments

We thank J. D. Cooper and S. S. Lefrak for numerous helpful conversations concerning lung physiology. We appreciate the assistance of G. A. Patterson and the Washington University Lung Transplant team, especially Nitin Das, for assistance with human donor lungs. We acknowledge the crucial contributions to this research from the lung donors and their families. The loan of a ^{3}He polarizer from General Electric is appreciated.

Y. V. Chang is currently affiliated with Children's Hospital of Philadelphia and S. T. Bartel with Washington University School of Medicine.

GRANTS

This research was funded by National Heart, Lung, and Blood Institute Grants R01 HL-70037 and R01 HL-72369.

References

1. Alex L, Dougherty L. MR imaging of motion with spatial modulation of magnetization. Radiology 1989;171:841–845. [PubMed: 2717762]

2. Bastacky J, Goerke J. Pores of Kohn are filled in normal lungs: low-temperature scanning electron microscopy. J Appl Physiol 1992;73:88–95. [PubMed: 1506404]
3. Berg, HC. Random Walks in Biology. Princeton, NJ: Princeton University Press; 1993.
4. Cai J, Altes TA, Miller GW, Sheng K, Read PW, Mata JF, Zhong X, Cates GD Jr, de Lange EE, Mugler JP 3rd, Brookeman JR. MR grid-tagging using hyperpolarized helium-3 for regional quantitative assessment of pulmonary biomechanics and ventilation. Magn Reson Med 2007;58:373–380. [PubMed: 17654579]
5. Cetti EJ, Moore AJ, Geddes GM. Collateral ventilation. Thorax 2006;61:371–373. [PubMed: 16648350]
6. Chen XJ, Hedlund LW, Möller HE, Chawla S, Maronpot RR, John-son GA. Detection of emphysema in rat lungs by using magnetic resonance measurements of ^{3}He diffusion. Proc Natl Acad Sci USA 2000;97:11478–11481. [PubMed: 11027348]
7. Conradi MS, Saam BT, Yablonskiy DA, Woods JC. Hyperpolarized He-3 diffusion MRI. Prog Nucl Magn Reson Spec 2006;48:63–83.
8. Conradi MS, Yablonskiy DA, Woods JC, Gierada DS, Bartel SET, Haywood SE, Menard C. The role of collateral paths in long-range diffusion of ^{3}He in lungs. Acad Rad. In press.
9. Haefeli-Bleuer B, Weibel ER. Morphometry of the human pulmonary acinus. Anat Rec 1988;220:401–414. [PubMed: 3382030]
10. Hogg JC, Macklem PT, Thurlbeck WM. The resistance of collateral channels in excised human lungs. J Clin Invest 1969;48:421–431. [PubMed: 5773080]
11. Inners CR, Terry PB, Traystman RJ, Menkes HA. Effects of lung volume on collateral and airway resistance in man. J Appl Physiol 1979;46:67–73. [PubMed: 457532]
12. Jensen JH, Helpern JA, Ramani A, Hanzhang L, Kaczynski K. Diffusion kurtosis imaging: the quantification of non-Gaussian water diffusion by means of magnetic resonance imaging. Magn Reson Med 2005;53:1432–1440. [PubMed: 15906300]
13. Kirchner B, Stubbs J, Marx D. Fast anomalous diffusion of small hydrophobic species in water. Phys Rev Lett 2002;89:215901–215904. [PubMed: 12443432]
14. Kitaoka H, Tamura S, Takaki R. A three-dimensional model of the human pulmonary acinus. J Appl Physiol 2000;88:2260–2268. [PubMed: 10846044]
15. Kundu, PK.; Cohen, IM. Fluid Mechanics. 2. New York: Academic; 2002.
16. Lambert MW. Accessory bronchiole-alveolar communications. J Pathol Bacteriol 1955;70:311–314. [PubMed: 13295905]
17. Leawoods JC, Yablonskiy DA, Saam BT, Gierada DS, Conradi MS. Hyperpolarized ^{3}He gas MR imaging. Concepts Magn Reson 2001;13:277–293.
18. Leawoods JC, Yablonskiy DA, Chino K, Tanoli TSK, Cooper JD, Conradi MS. Magnetization tagging decay to measure long-range ^{3}He diffusion in healthy and emphysematous canine lungs. Magn Reson Med 2004;51:1002–1008. [PubMed: 15122683]
19. Lide, DR. CRC Handbook of Chemistry and Physics. 85. Boca Raton, FL: CRC; 2004. p. 8-87.
20. Macklem PT. Airway obstruction and collateral ventilation. Physiol Rev 1971;51:368–436. [PubMed: 4928122]
21. Macklem PT. Collateral ventilation. N Engl J Med 1978;298:49–50. [PubMed: 618452]
22. Martin HB. Respiratory bronchioles as the pathway for collateral ventilation. J Appl Physiol 1966;21:1443–1447. [PubMed: 5923213]
23. Mathews, J.; Walker, RL. Mathematical Methods of Physics. Menlo Park, CA: Benjamin; 1970. p. 217-252.
24. Menkes, HA.; Macklem, PT. Handbook of Physiology. The Respiratory System. Vol. sect 3. Bethesda, MD: Am. Physiol. Soc; 1977. Collateral flow; p. 337-353.
25. Möller HE, Chen XJ, Saam B, Hagspiel KD, Johnson GA, Altes TA, de Lange EE, Kauczor HU. MRI of the lungs using hyperpolarized noble gases. Magn Reson Med 2002;47:1029–1051. [PubMed: 12111949]
26. Morbach AE, Gast KK, Schmiedeskamp J, Dahmen A, Herweling A, Heussel CP, Kauczor HU, Schreiber WG. Diffusion-weighted MRI of the lung with hyperpolarized helium-3: a study of reproducibility. J Magn Reson Imaging 2005;21:765–774. [PubMed: 15906344]

27. Owers-Bradley JR, Bennattayalah A, Fichele S, McGloin JC, Bowtell R, Morgan PS, Moody AR. Diffusion and tagging of hyperpolarized ^{3}He in the lungs (Abstract). Proc Int Soc Magn Reson Med 2002;10:2016.
28. Saam BT, Yablonskiy DA, Kodibagkar VD, Leawoods JC, Gierada DS, Cooper JD, Lefrak SS, Conradi MS. MR imaging of diffusion of He-3 gas in healthy and diseased lungs. Magn Reson Med 2000;44:174–179. [PubMed: 10918314]
29. Salerno M, de Lange EE, Altes TA, Truwit JD, Brookeman JR, Mugler JP. Emphysema: hyperpolarized helium 3 diffusion MR imaging of the lungs compared with spirometric indexes—initial experience. Radiology 2002;222:252–260. [PubMed: 11756734]
30. Schreider JP, Raabe OG. Structure of the human respiratory acinus. Am J Anat 1981;162:221–232. [PubMed: 7315750]
31. Terry PB, Traystman RJ, Newball HH, Batra G, Menkes HA. Collateral ventilation in man. N Engl J Med 1978;298:10–15. [PubMed: 618444]
32. Verbanck S, Paiva M. Simulation of the apparent diffusion of helium-3 in the human acinus. J Appl Physiol 2007;103:249–254. [PubMed: 17379747]
33. Wang C, Miller GW, Altes TA, de Lange EE, Cates GD Jr, Mugler JP 3rd. Time dependence of ^{3}He diffusion in the human lung: measurement in the long-time regime using stimulated echoes. Magn Reson Med 2006;56:296–309. [PubMed: 16791861]
34. Wang C, Altes TA, Miller GW, de Lange EE, Ruppert K, Brookeman JR, Mata JF, Cates GD Jr, Mugler JP 3rd. Short-time-scale and long-time-scale ^{3}He diffusion MRI in emphysema: which is more sensitive? (Abstract). Proc Int Soc Magn Reson Med 2007;15:941.
35. Weibel, ER. Design of airways and blood vessels considered as branching trees. In: Crystal, RG.; West, JB.; Barnes, PJ.; Weibel, ER., editors. The Lung: Scientific Foundations. 2. Philadelphia, PA: Lippincott-Raven; 1997. p. 1061-1071.
36. West, JB. Pulmonary Pathophysiology. 4. Baltimore, MD: Williams & Wilkins; 1992. p. 58-62.
37. West, JB. Respiratory Physiology. 5. Baltimore, MD: Williams & Wilkins; 1995. p. 21-30.
38. Woods JC, Choong CK, Yablonskiy DA, Chino K, Macklem PT, Pierce JA, Cooper JD, Conradi MS. Long-range diffusion of hyperpo-larized ^{3}He in excised normal and emphysematous human lungs via magnetization tagging. J Appl Physiol 2005;99:1992–1997. [PubMed: 16024528]
39. Woolcock AJ, Macklem PT. Mechanical factors influencing collateral ventilation in human, dog, and pig lungs. J Appl Physiol 1971;30:99–115. [PubMed: 5538799]
40. Yablonskiy DA, Sukstanskii AL, Leawoods JC, Gierada DS, Bret-thorst GS, Lefrak SS, Cooper JD, Conradi MS. Quantitative in vivo assessment of lung microstructure at the alveolar level with hyperpolarized ^{3}He diffusion MRI. Proc Natl Acad Sci USA 2002;99:3111–3116. [PubMed: 11867733]

APPENDIX

We consider here the attenuation of modulated magnetization due to diffusion entirely within individual acini; we show that this attenuation is limited and small for the wavelengths used in the present study.

We first approximate acini as 185-mm^3 cubes, so the edge length L is 0.57 cm. For simplicity, we orient one of the cube edges parallel to the gradient direction (x). Displacements of ^{3}He spins are limited by the box size. The probability $P(u)$ of displacements of (signed) length u is (in the infinite time limit)

$$P(u)=\int_x a(x)a(x+u)dx \tag{A1}$$

where $a(x)$ is the normalized cross-sectional area of the acinus. In the cube model, the cross section is constant

$$a(x)=\begin{cases}\frac{1}{L}, & 0\le x\le L\\ 0, & otherwise\end{cases} \tag{A2}$$

$P(u)$ is the "house-top" function displayed in Fig. 8. $P(u)$ is only nonzero for $-L \le u \le L$, inasmuch as displacements of larger magnitude than L are impossible. We note that $P(u)$ approaches 0 as u approaches L, because displacements of length L are unlikely, requiring a spin start at the left wall and finish at the right wall.

The initial spatially modulated magnetization is taken as $\cos(kx)$, with $k = 2\pi/\lambda$. In the limit of long times, the magnetization within each acinus becomes uniform, through intra-acinar diffusion. The resulting spin magnetization averaged over all acini is then the convolution (23) of the $\cos(kx)$ input function with the displacement probability $P(u)$

$$\mathrm{M}(x)=\int_{all x_1}\cos(kx_1)P(x-x_1)\mathrm{d}x_1=\int_{all u}\cos[k(x-u)]P(u)\mathrm{d}u \tag{A3}$$

In the cubemodel, this becomes $\mathrm{M}(x) = \alpha\cos(kx)$, where the amplitude factor (α) is

$$\alpha=[\sin(kL/2)/(kL/2)]^2=[\mathrm{sinc}(kL/2)]^2 \tag{A4}$$

For $\lambda = 2$ cm and $L = 0.57$ cm, $\alpha = 0.737$. Thus complete diffusion within each acinus can only attenuate the modulated magnetization by 26%, much less than what is observed. For longer wavelengths, even less attenuation is possible. This conclusion is qualitatively evident from Fig. 8, where the width of the spreading function P is clearly seen to be only comparable to that of the initial cosine modulation function.

A somewhat more realistic acinar model for the present purposes is a sphere of radius R. To account for the same acinar volume, $R = 0.353$ cm. The "shape" of the sphere, its projection onto the x-axis, is

$$a(x)=\begin{cases}[3/(4R^3)](R^2-x^2), & |x|\le R\\ 0, & otherwise\end{cases} \tag{A5}$$

We note that this $a(x)$ is properly normalized. The resulting probability of displacements (in the x direction) of signed length u, $P(u)$, is presented in Fig. 8. Although it has somewhat longer tails than for the cube model, its overall width is slightly narrower. Convolution of the spherical model $P(u)$ with the input function $\cos(kx)$ as in Eq. A3 leads to α

$$\alpha=[\mathrm{sinc}_{3D}(kR)]^2 \tag{A6}$$

where the 3D sinc function is given by

$$\mathrm{sinc}_{3D}(Z)=3(\sin Z - Z\cos Z)/Z^3 \tag{A7}$$

Using $\lambda = 2$ cm and $R = 0.353$ cm, $\alpha = 0.778$; this is slightly less attenuation than for the cube model.

These calculations confirm that diffusion of ^{3}He within individual acini can only produce a small attenuation of the modulated magnetization for ≥2-cm wavelengths. Further attenuation requires diffusion between different acini.

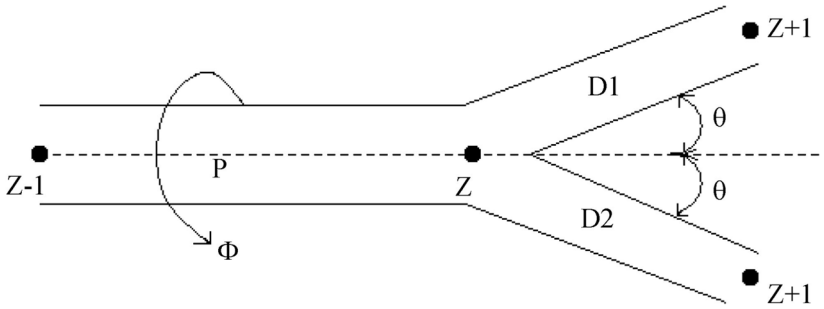

Fig. 1.

Geometry of branching airways. P, parent airway of *Z*th level node; D1 and D2, daughter airways and nodes (all numbered level $Z + 1$); θ, half-angle of branching; φ, angle of rotation of the P-D1–D2 plane about the parent airway. Nodes are labeled by their level.

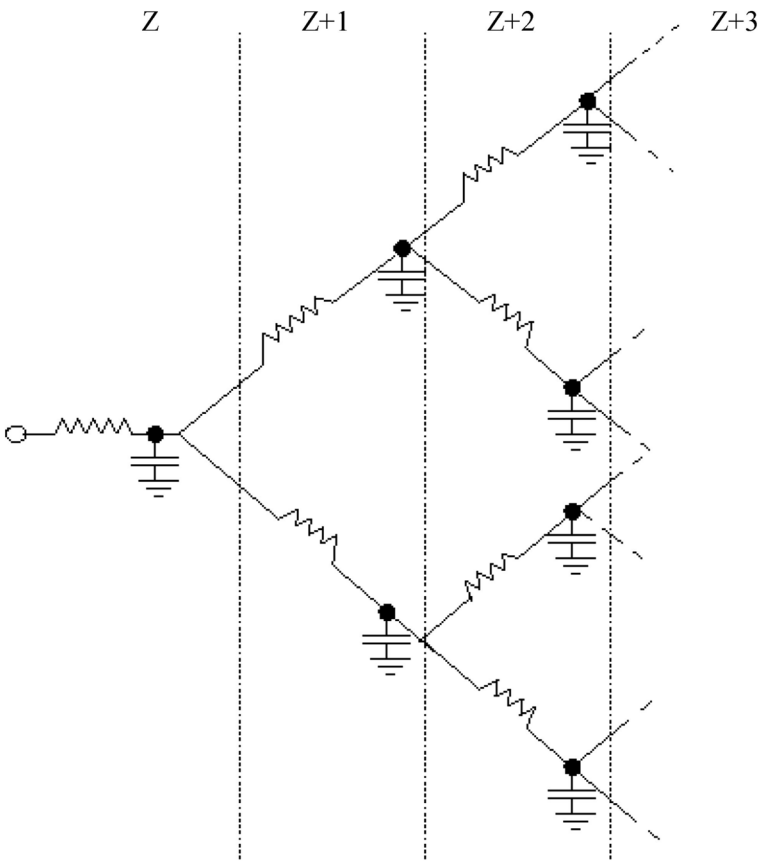

Fig. 2.
Resistor-capacitor electrical network analog to the branching airways of the lung. Resistors represent airways and capacitors represent airway nodes. Analogous quantities (diffusing spins vs. electrical resistor-capacitor) are given in Table 1. All resistors and capacitors of a given level are equal (symmetrical branching model). Levels of branching are labeled at *top*.

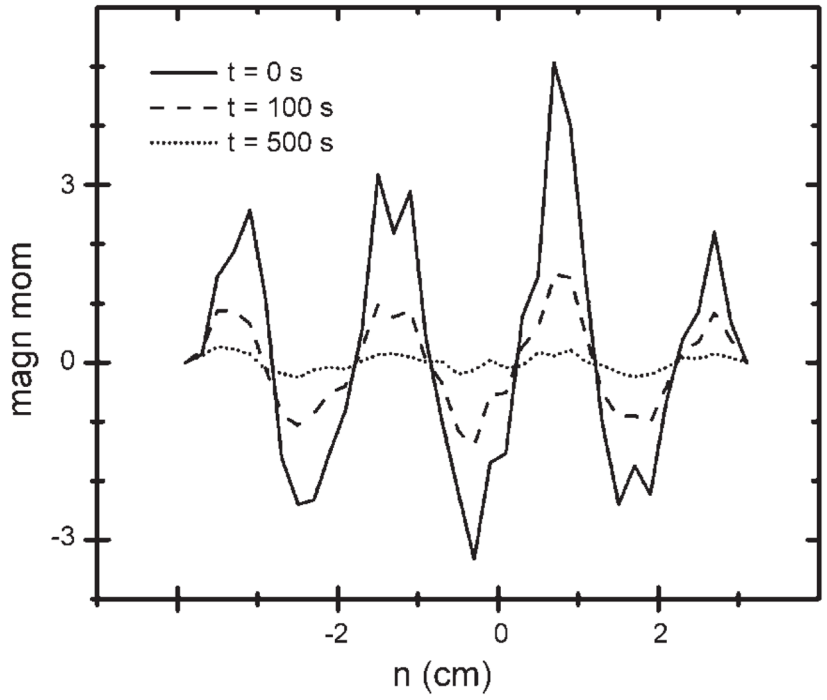

Fig. 3.
Magnetic moment as a function of coordinate *n* (−4 to 3 cm), the projection of each acinar node's position onto the direction of the striping gradient.

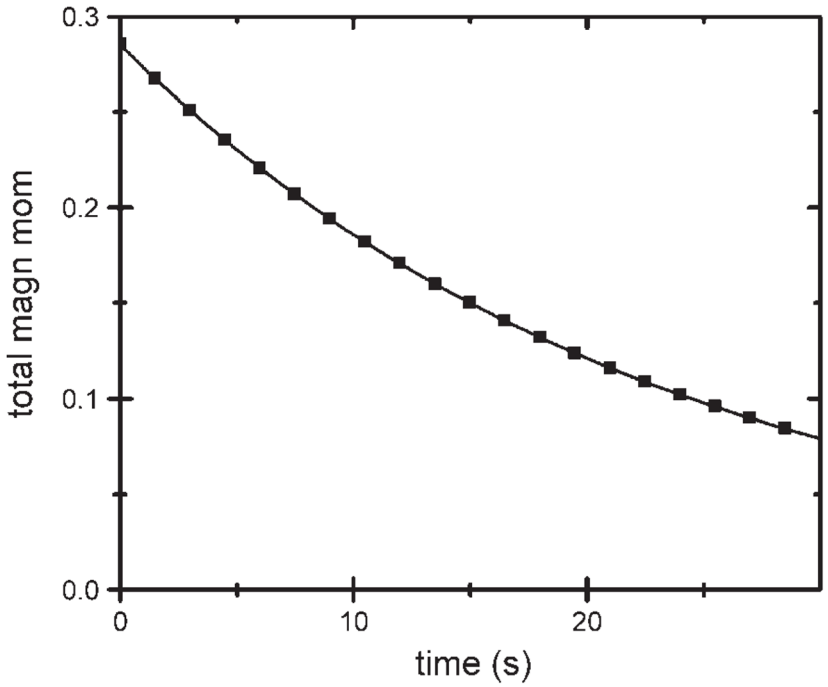

Fig. 4.

Decay of total magnetic moment in a simulated acinus that is allowed to freely exhaust by diffusion at time ≥0. Solid curve is a single-exponential fit with decay time constant of 23 s.

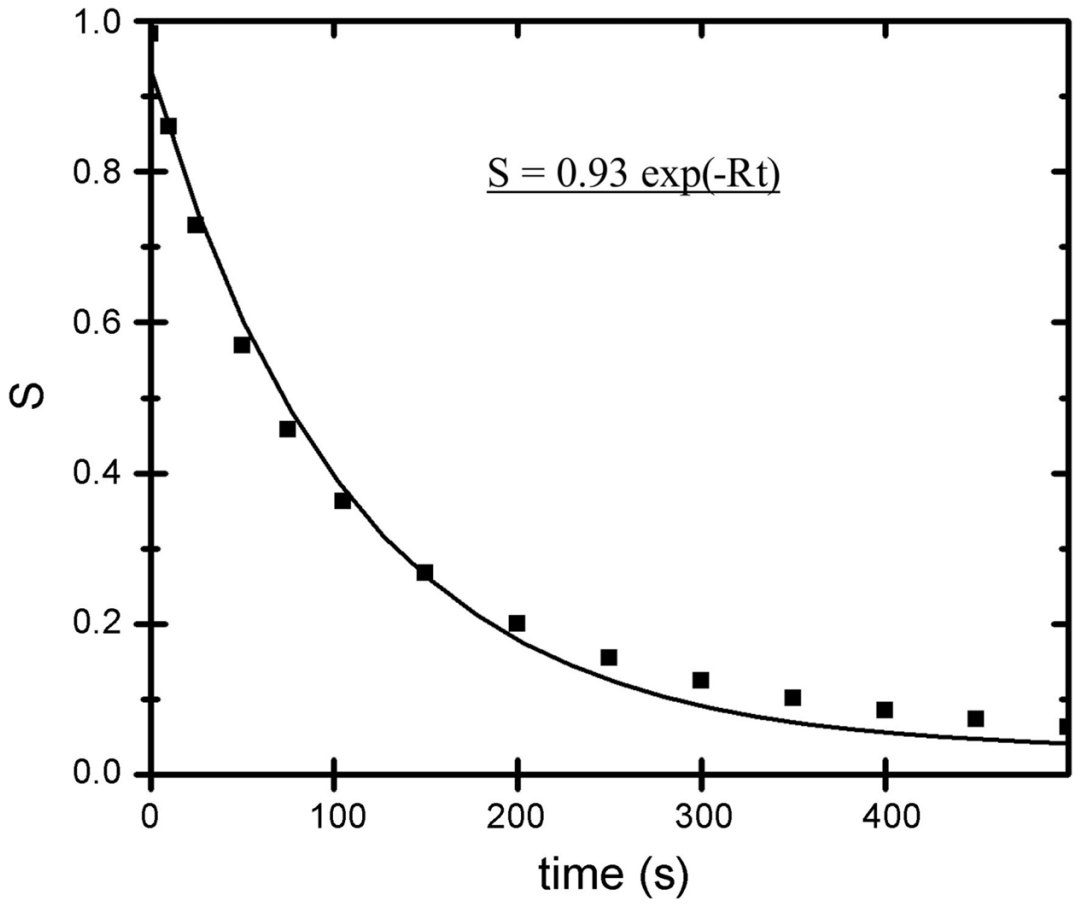

Fig. 5.

Decay of the amplitude of modulated magnetization (S) as a function of time for a simulated lung. Solid curve shows single-exponential fit with rate constant (R) = 110 s^{-1}.

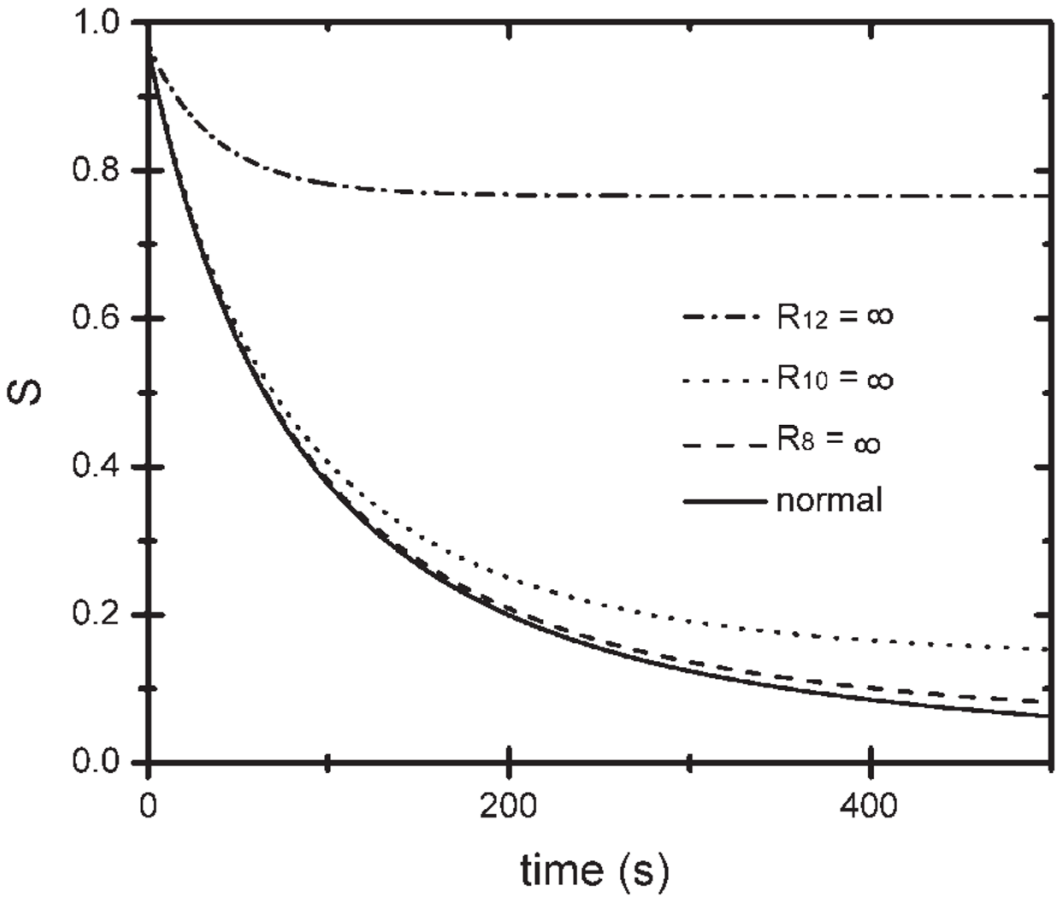

Fig. 6.

Decay of S as a function of time for a normal simulated lung and lungs with all airways of a given level (level 8, 10, or 12) closed. Very few diffusion paths relevant to the decay of λ = 2 cm stripes pass through level 8 or 10 airways, but most pass through level 12 airways.

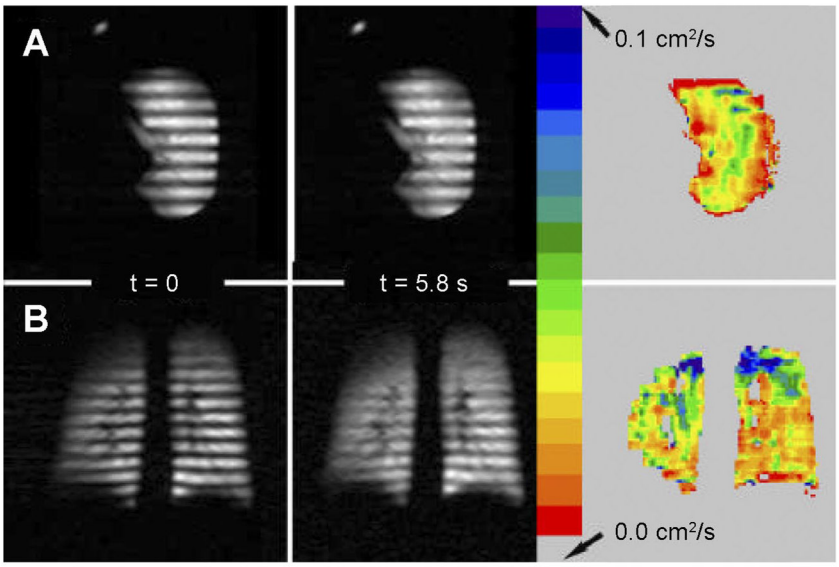

Fig. 7.

Magnetization-striped images from a normal donor lung (*A*, Ex Vivo3 in Table 2) and a healthy volunteer (*B*, In Vivo1 in Table 2). Images are the first ($t = 0$) and last ($t = 5.8$ s) of a series of such images. Color bar refers to maps of LRADC calculated from time decay of modulation. Explanted lung images are oriented approximately axially, with anterior at *top*, posterior at *bottom*, and medial at *left*.

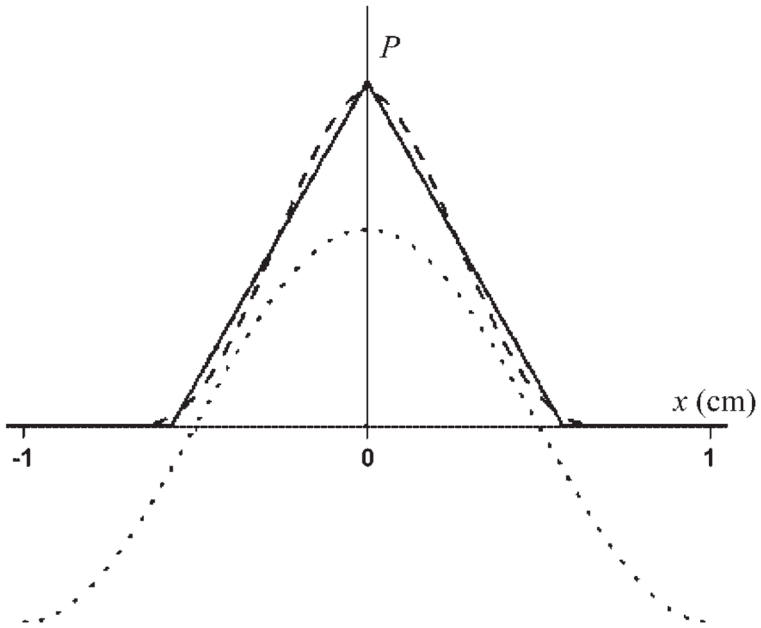

Fig. 8.

Probabilities (P) of displacements (x) restricted to single acini for the cube model (solid curve) and sphere model (dashed curve), both corresponding to 185-mm^3 acinar volumes. Functions P are limited by the physical sizes of the acini, so they are nonzero only for $-L \leq x \leq L$ and $-2R \leq x \leq 2R$, respectively. Function $\cos(kx)$ is also presented for $\lambda = 2$ cm (dotted curve). Vertical scale is arbitrary.

Table 1

Analogous quantities and equations linking diffusion of magnetic moments and RC network of Fig. 2

Diffusing Spins	**Electrical**
Magnetic moment (μ)	Charge (*q*)
Magnetization (M)	Voltage (*V*)
Volume (V)	Capacitance (*C*)
M = μ/V	$V = q/C$
Flow of magnetic moment (*I*)	Current (*I*)
Diffusion equation: $I = (D\Delta M/L)A$	$I = \Delta V/R$
DA/L	$1/R$
Continuity equation: $dM/dt = (1/V)I_{tot}$	$dV/dt = (1/C)I_{tot}$

A and *L*, airway cross-sectional area and length; V, volume associated with a node ($V = AL$); I_{tot}, total current flowing into a node along the parent and 2 daughter airways or resistors. Each current (magnetic moment per time) equals difference in M between neighboring nodes (ΔM) times diffusive conductance (DA/L).

Table 2

Long-range diffusivity measurements

	Sex	Age, yr	λ, cm	⟨LRADC⟩, cm^2/s	Apex	Base
Ex Vivo1	F	30	3	0.025		
Ex Vivo2	M	21	2	0.029	0.035	0.027
Ex Vivo3	M	21	2	0.019	0.022	0.017
Ex Vivo4	M	22	2	0.009	0.012	0.007
Ex Vivo5	F	40	3	0.015	0.024	0.011
In Vivo1	M	31	2	0.048	0.074	0.037
In Vivo2	M	26	2.8	0.026	0.031	0.022
In Vivo3	M	23	2.1	0.042	0.047	0.038
Low vol			2.1	0.035	0.040	0.023
In Vivo4	F	25	2.8	0.027	0.058	0.010
Low vol			2.8	0.017	0.048	0.010
PIG1			2.1	0.0051		
PIG2			2.1	0.0039		
PIG3			2.1	0.0040		
FIXPIG			2.1	0.0048		

For In Vivo3 and In Vivo4, measurements were made at nearly full inhalation and near functional reserve capacity (“low vol”). All long-range apparent diffusion coefficient (LRADC) values have ±10% precision. λ, Wavelength.